ACS MATERIALS Au
AN OPEN ACCESS JOURNAL OF THE AMERICAN CHEMICAL SOCIETY

pubs.acs.org/materialsau
Article

Chemical Origins of Optically Addressable Spin States in $Eu_2(P_2S_6)$ and $Eu_2(P_2Se_6)$

Published as part of ACS Materials Auspecial issue"2024 Rising Stars".

Uchenna V. Chinaegbomkpa, Xudong Huai, Michal J. Winiarski, Hugo Sanabria, and Thao T. Tran*

Cite This: https://doi.org/10.1021/acsmaterialsau.4c00102
Read Online

ACCESS | Metrics & More | Article Recommendations | Supporting Information

ABSTRACT: Lanthanide materials with a $4f^7$ electron configuration ($^8S_{7/2}$) offer an exciting system for realizing multiple addressable spin states for qubit design. While the $^8S_{7/2}$ ground state of $4f^7$ free ions displays an isotropic character, breaking degeneracy of this ground state and excited states can be achieved through local symmetry of the lanthanide and the choice of ligands. This makes Eu^{2+} attractive as it mirrors Gd^{3+} in exhibiting the $^8S_{7/2}$ ground state, capable of seven spin-allowed transitions. In this work, we identify $Eu_2(P_2S_6)$ and $Eu_2(P_2Se_6)$ as viable candidates for optically addressable spin states. The materials feature paramagnetic behavior at $2.0 \leq T \leq 400$ K and $\mu_0 H = 0.01$ and 7 T. The field-dependent magnetization $M(H)$ curve reveals a single-ion spin with effective magnetic moments comparable to the expected magnetic moment of Eu^{2+}. Seven well-defined narrow peaks in the excitation and emission spectra of Eu^{2+} are resolved. Phonon contributions to the Eu^{2+} spin environment are evaluated through heat capacity measurements. Insights into how the spin-polarized band structure and density of states of the materials influence the physical properties are described by using density functional theory calculations. These results present a foundational study of $Eu_2(P_2S_6)$ and $Eu_2(P_2Se_6)$ as a feasible platform for harnessing the spin, charge, orbital, and lattice degrees of freedom of Eu^{2+} for qubit design.

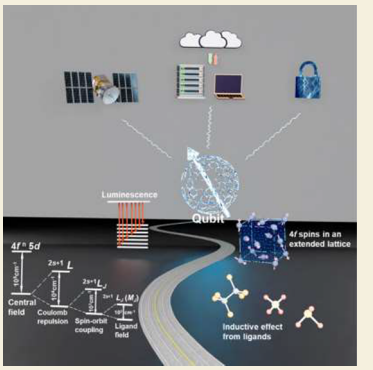

KEYWORDS: *europium, chalcogenophosphates, photoluminescence, paramagnetism, light−matter interactions, ligand field*

INTRODUCTION

Lanthanide complexes in various coordination frameworks lend themselves as tunable candidates for quantum information science, especially in spin qubits design.[1−13] This derives from the demonstrated implementation of Grover's algorithm using single magnetic molecules[2,3,10,14] and from the feasibility of chemically optimizing quantum coherence in such molecules.[15,16] It also draws from the ease of atomic precision and the unmatched scalability inherent in molecular synthesis.[4,6,15,17−19] The specific electronic configuration with great potential to incorporate tunability and scalability is the $4f^7$ electron configuration, such as Eu^{2+}, Gd^{3+}, and Tb^{4+}.[6,7,20] Though isotropic in character, the well-isolated $^8S_{7/2}$ ground state and the associated seven allowed transitions can be explored toward engineering qubits with multiple addressable energy levels, potentially enabling scalability of the number of qubits available for implementing quantum algorithms in a single molecule.[4,6] Such multilevel qubit systems have been reported for Gd^{3+}, where the seven allowed transitions of the multiplet $^8S_{7/2}$ ground state were individually addressed and coherently manipulated.[21−24] With regard to Eu^{2+}, only a few studies have been reported, suggesting that Eu^{2+} systems provide an excellent playground for multilevel qubit candidates.[25,26] The uniqueness of Eu^{2+} includes the large nuclear spin ($I = 5/2$), and the mixing of the excited state manifolds upon excitation.[27] Critically, nuclear spins are more detrimental to spin qubits when they constitute a large portion of the qubit's environment, as obtained for complexes rich in nitrogen, halogen, and hydrogen.[5,28] For the lanthanoid's nuclear spin, the strong coupling to the electronic spin minimizes the odds of decoherence arising from a spin bath. For isotope purity, the two naturally occurring isotopes of europium, ^{153}Eu and ^{151}Eu, are of almost equal abundance (0.5219 and 0.4781 mol fractions, respectively) and possess the same spin and parity.[29] Eu^{2+} coordination complexes enable an impressive approach for engineering multiple qubits attributable to their tunability and controllability. However, their primary challenges are the coupling of several excited-state manifolds and the ready oxidation to Eu^{3+} in most coordination complexes. The excited-state coupling, arising from the spin-allowed 4f−5d electronic transitions, merges the

Received: August 31, 2024
Revised: October 21, 2024
Accepted: October 21, 2024

well-defined 7 electronic transitions into a continuum. This typically results in broad excitation and emission bands in the photoluminescence (PL) spectra of Eu^{2+}.[30] However, for stoichiometric compounds of Eu^{2+}, the fine structure of the 4f−5d transitions can be resolved, and the +2 oxidation state is more preserved in the solid state.[31]

In this work, we present $Eu_2(P_2L_6)$ (L = S, Se) as a viable extended solid platform to study the spin, orbital, and electron degrees of freedom of Eu^{2+} and report our findings on the magnetic and optical properties of the materials. We propose that placing Eu^{2+} $4f^7$ with a C_{2v} point group symmetry in a stoichiometric system will achieve magnetically isolated spins while resolving the characteristic seven allowed transitions in PL. This can enable a uniform array of spin centers on an extended framework. We assess the impact of symmetry, crystal field, and chemical bonds on the physical properties of $Eu_2(P_2L_6)$. The extent of lattice perturbations to the spin environment of Eu^{2+} and the presence of any phase transitions are evaluated using heat capacity measurement. The UV−vis−NIR absorption and Fourier transform infrared (FTIR) spectral features of $Eu_2(P_2L_6)$ are presented to describe their optical band gaps and bonding vibrations. We also draw insights into how the spin-polarized (SP) band structure and density of states of the materials influence their physical properties by using density functional theory (DFT) calculations.

EXPERIMENTAL SECTION

Synthesis

$Eu_2(P_2L_6)$ (L = S, Se) was synthesized using the KI flux method reported by Huang and co-workers.[32] Eu pieces (sublimed dendritic 99.9% (REO), Alfa Aesar), phosphorus (99% trace metal basis, Aldrich), precipitated sulfur (anhydrous basis, 99.5−100.5%, Spectrum chemical), selenium (325 mesh, 99.5% metal basis, Thermo Scientific), and phosphorus pentasulfide (98+%, Thermo Scientific) were combined to obtain the molar ratio of 1:1:3 for the elements in $Eu_2(P_2S_6)$ and $Eu_2(P_2Se_6)$, respectively. The starting materials and 400 mg of KI (99.9% metal basis, Thermo Scientific) were loaded into a quartz tube in a glovebox and carefully double-sealed under vacuum. The reactions were ramped to 960 °C in 46.75 h for $Eu_2(P_2S_6)$ and 750 °C in 31.25 h for $Eu_2(P_2Se_6)$ in a muffle furnace, allowed to dwell for 48 h, and cooled at 2 °C/h to room temperature.

Phase Analysis

The crystal structure of $Eu_2(P_2L_6)$ was confirmed by single-crystal X-ray diffraction (XRD) collected on an XtaLAB Synergy-Dualflex-HyPix diffractometer with the radiation wavelength (Mo Kα) set to 0.71073 Å. Unit cell determination, reduction, scaling, and absorption corrections were performed using the CrysAlisPro 1.171.42.89a. software.[33] The crystal structures were solved using the dual methods on the ShelXT program.[34] The phase purity of the samples was evaluated from powder XRD data collected on a Bruker D2 Phaser diffractometer equipped with a LynxEye-XE-T detector. Rietveld refinement was achieved using the Topas Academic V6 software.[35]

Thermogravimetric Analysis

The thermal behavior of $Eu_2(P_2S_6)$ and $Eu_2(P_2Se_6)$ was investigated via simultaneous thermal analysis (TGA/DSC) from T = 273−1273 K (Figure S3). Data collection was achieved under a constant flow of nitrogen, with heating and cooling rates set at 10 °C/min.

Spectroscopic Measurements

The UV−vis−NIR absorption spectra and FTIR spectra of $Eu_2(P_2L_6)$ (L = S, Se) were obtained using an Agilent Cary UV−vis (NIR) 7000 spectrophotometer at 350 nm $\leq \lambda \leq$ 3000 nm and a Shimadzu IR Affinity-1S at 400 $cm^{-1} \leq \nu \leq$ 4000 cm^{-1}, respectively. The transmission mode was employed, and transparent pellets were made using 100 mg of KBr and 0.5 mg of samples. For the photoluminescence measurements, thin layers of the $Eu_2(P_2L_6)$ samples were prepared by drop-casting a methanol suspension of the sample on a quartz substrate. Temperature-dependent steady-state measurements at 78 K $\leq T \leq$ 400 K were performed by using a HORIBA Nanolog spectrofluorometer equipped with a xenon lamp (HORIBA FL-1039) and a CCD detector (HORIBA Symphony II). The sample chamber was housed in a cryostat evacuated to $\sim 10^{-6}$ Torr and thermally monitored using a Lake Shore (model 325) temperature controller. The time-resolved photoluminescence measurement was achieved using a HORIBA FluoroLog FL3−22 spectrofluorometer equipped with a picosecond photon detection module (TBX-05), a single photon-counting controller (FluoroHub-B) assisted with an external NanoLED driver, and a 375 nm laser source (NanoLED N-375L).

Physical Property Measurements

DC magnetization measurements were performed using 14.5 mg of $Eu_2(P_2S_6)$ and 20.8 mg of $Eu_2(P_2Se_6)$. The vibrating sample magnetometer option of Quantum Design Physical Properties Measurement System (PPMS) was employed. Temperature-dependent data, $M(T)$, was collected at 2 K $\leq T \leq$ 400 K under an applied magnetic field of 0.01 and 7 T, while variable-field data, $M(H)$, was collected at T = 2 and 10 K. $M(T)$ data sets include zero-field-cooled and field-cooled measurements. For heat capacity, measurements were conducted using the semiadiabatic pulse technique of PPMS at 2 K $\leq T \leq$ 230 K.

Density Functional Theory Calculations

The DFT SP + spin−orbit coupling calculations were performed using a full-potential linearized augmented plane-wave method as implemented in the WIEN2k code.[36] The exchange and correlation energies were treated within the Perdew−Burke−Ernzerhof generalized gradient approximation.[37] The muffin-tin radius values of 2.35, 2.04, 2.0, and 1.85 Bohr were used for the Eu, Se, S, and P atoms, respectively. Energy convergence was set at 0.0001 and achieved at 0.00009. The self-consistent field calculations were completed on a 5 × 5 × 4 k-point mesh.

RESULTS AND DISCUSSION

Crystal Structure

$Eu_2(P_2L_6)$ (L = S, Se) crystallizes in a centrosymmetric monoclinic structure (space group $P2_1/c$) (Figure 1 and Table S1).[38,39] The $[P_2L_6]^{4-}$ anions display a staggered ethane-like conformation with a D_{3d} symmetry.[38−41] (Figure S1). The Eu^{2+} cations are connected to the $[P_2L_6]^{4-}$ groups through edge-sharing and face-sharing Eu−L bonds, forming a three-dimensional structure.[39,40] Each Eu^{2+} coordinates with eight S or Se atoms to form a bicapped trigonal prism with a C_{2v} point group.[32,39,42] The Eu−L bond lengths range from 3.0270(8) to 3.1681(7) Å for $Eu_2(P_2S_6)$ and from 3.1433(12) to 3.3131(7) Å for $Eu_2(P_2Se_6)$ (Figure S2). The Eu^{2+} ions form a symmetric one-dimensional zigzag chain along the b-axis (Figure 1). The Eu−Eu distances are 4.6404(3) Å and 4.8463(9) Å in $Eu_2(P_2S_6)$ and $Eu_2(P_2Se_6)$, respectively.[39,40] Both compounds are thermally stable up to 1073 K for $Eu_2(P_2S_6)$ and 973 K for $Eu_2(P_2Se_6)$ (Figure S3).

Magnetization Studies

Although some results on the magnetic property of $Eu_2(P_2S_6)$ were reported,[32,39] that of $Eu_2(P_2Se_6)$ and a comparison between the materials remains to be explored. DC magnetization measurements at 2.0 K < $T \leq$ 400 K, $\mu_0 H$ = 0.01, and 7 T showed a paramagnetic behavior for $Eu_2(P_2X_6)$ and no magnetic phase transition down to T = 1.8 K (Figures 2a,b, S4, and S5). The Curie−Weiss analysis of the high-temperature data (100 $\leq T \leq$ 400 K) yielded an effective magnetic moment

https://doi.org/10.1021/acsmaterialsau.4c00102
ACS Mater. Au XXXX, XXX, XXX−XXX

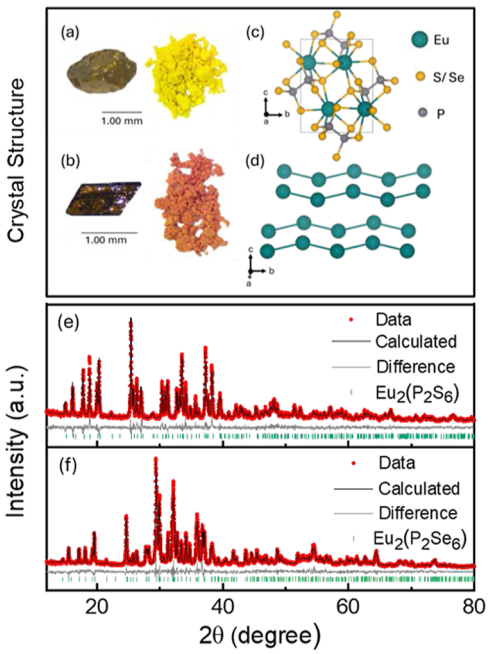

Figure 1. (a,b) Crystals and powder of $Eu_2(P_2S_6)$ and $Eu_2(P_2Se_6)$, respectively. (c,d) Crystal structure and one-dimensional Eu−Eu zigzag chain in $Eu_2(P_2S_6)$ and $Eu_2(P_2Se_6)$. (e,f) Powder XRD data of $Eu_2(P_2S_6)$ and $Eu_2(P_2Se_6)$, respectively.

of 7.522 μ_B/Eu^{2+} for $Eu_2(P_2S_6)$ and 7.664 μ_B/Eu^{2+} for $Eu_2(P_2Se_6)$. The moments are comparable to 7.94 μ_B, the expected magnetic moment of a Eu^{2+} free ion (S = 7/2, L = 0, and J = 7/2), and g = 2.0023. The nearly zero Curie−Weiss temperatures, θ_{CW} = −0.088 K for $Eu_2(P_2S_6)$ and θ_{CW} = 0.782 K for $Eu_2(P_2Se_6)$, indicate small to negligible exchange interactions between the Eu^{2+} spins. We measured magnetization (M) as a function of magnetic field (H) from μ_0H = 0−7 T and compared the data to the magnetic moment of an ideal paramagnet with total angular momentum, J, as described in eqs 2−4.[43]

$$M_J = Ng\mu_B \boldsymbol{J} B_J(x) \tag{2}$$

where the Brillouin function, B_J, is defined as

$$B_J(x) = \frac{2J+1}{2J}\coth\left(\frac{(2J+1)x}{2J}\right) - \frac{1}{2J}\coth\left(\frac{x}{2J}\right) \tag{3}$$

x, the ratio of the Zeeman energy in the magnetic moment of the external field to the thermal energy k_BT, is expressed as

$$x = \boldsymbol{J}\frac{g\mu_B B}{K_B T} \tag{4}$$

N is the number of Eu^{2+} ions per unit volume, g is the Lande g-factor, μ_B is the Bohr magneton, K_B is the Boltzmann constant, and T is the temperature. The $M(H)$ curves of $Eu_2(P_2L_6)$ at T = 2 K somewhat follow the Brillouin function and approach saturation at around μ_0H = 6 T (Figures 2c and S6). This suggests nearly noninteracting to weakly interacting spin systems. The Se compound displays more deviation from the Brillouin function at 0 ≤ μ_0H ≤ 3 T than the S material. This can be attributed to the more dispersed Se-4p bands mediating Eu^{2+} spin−spin interactions.

Heat Capacity Studies

To investigate the thermodynamic signatures of $Eu_2(P_2L_6)$, we measured the heat capacity at μ_0H = 0, 6, and 9 T (Figure S7). The C_p/T vs T curves at μ_0H = 0 T show no anomalies

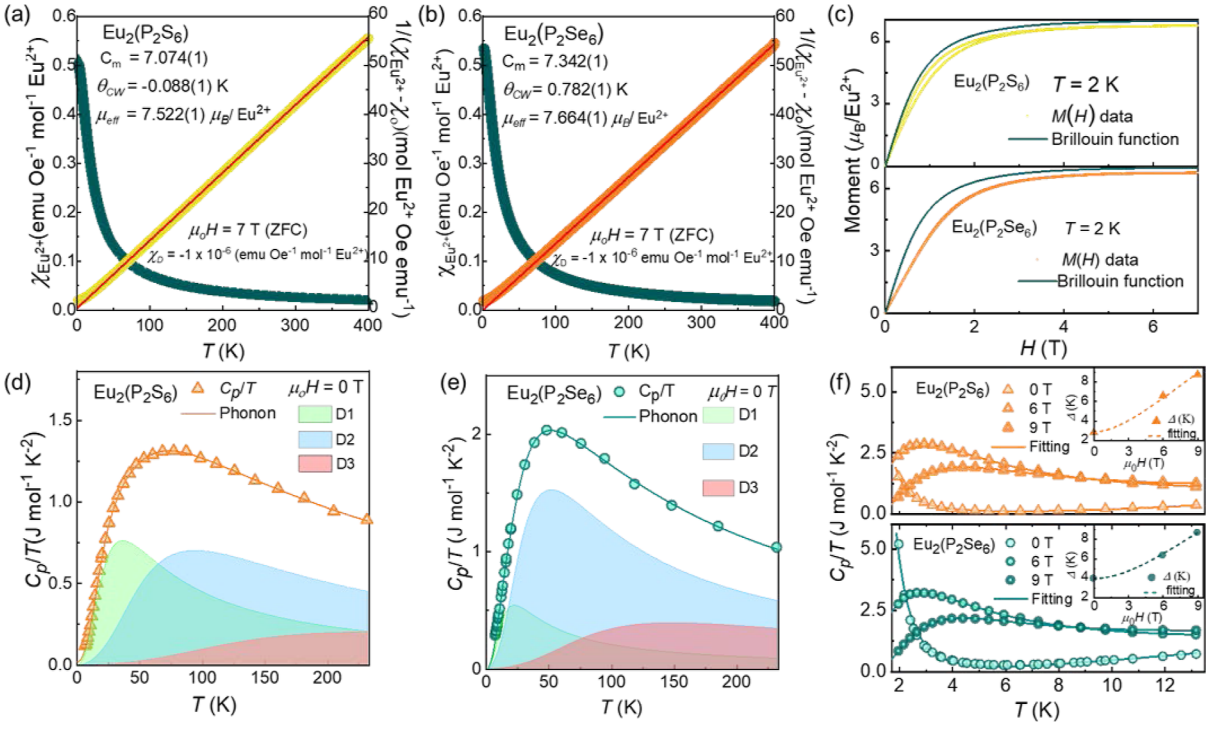

Figure 2. $Eu_2(P_2S_6)$ and $Eu_2(P_2Se_6)$: (a,b) magnetic susceptibility, $\chi(T)$ at 1.8 K ≤ T ≤ 400 K. The Curie−Weiss fitting spans from 100 K ≤ T ≤ 400 K. The line was extended to the axis to guide the eye. (c) $M(H)$ curves from 0 T − 7, at T = 2 K. (d,e) Heat capacity C_p/T vs T at μ_0H = 0 T, T = 2−230 K. (f) Analysis of the Schottky anomaly. The insets show that Δ (K) increases with increasing μ_0H (T).

https://doi.org/10.1021/acsmaterialsau.4c00102
ACS Mater. Au XXXX, XXX, XXX−XXX

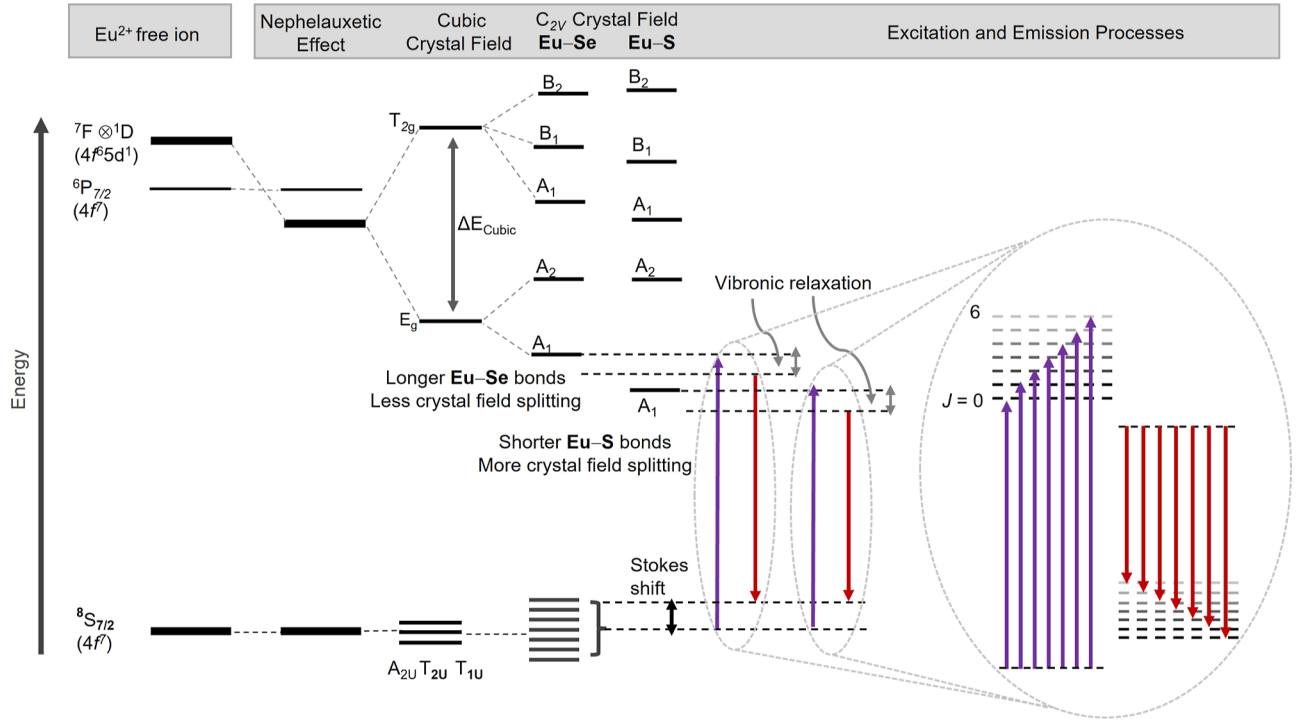

Figure 3. Proposed energy band diagram showing the impact of symmetry, crystal field, and bonding on the excitation and emission processes of $Eu_2(P_2L_6)$ (L = S, Se). Eu−S bonds are shorter than Eu−Se bonds, resulting in a larger crystal field splitting in $Eu_2(P_2S_6)$ than in $Eu_2(P_2Se_6)$.

associated with magnetic phase transitions, the supporting magnetization results (Figure 2d–f). For solids at low temperatures, we assume[44]

$$\frac{C_P}{C_V} \approx 1 \tag{5}$$

The heat capacity data were analyzed by decoupling the phonon into its constituent modes. A combination of three Debye modes (eq 6) was used to fit the data.[44]

$$C_P(T) = C_{D1}(\theta_{D1}, s_{D1}, T) + C_{D2}(\theta_{D2}, s_{D2}, T) + C_{D3}(\theta_{D3}, s_{D3}, T) \tag{6}$$

$$C_D(\theta_D, T) = 9 s_D R \left(\frac{T}{\theta_D}\right)^3 \int_0^{\theta_D/T} \frac{(\theta_D/T)^4 e^{(\theta_D/T)}}{[e^{(\theta_D/T)} - 1]^2} d\frac{\theta_D}{T} \tag{7}$$

where θ_D is the Debye temperature, R is the gas constant, and s_D is the number of oscillators for each Debye mode.

The fitting parameters are summarized in Table S8. The total number of oscillators is 10.07 for $Eu_2(P_2S_6)$ and 10.58 for $Eu_2(P_2Se_6)$, comparable to the number of atoms in each formula unit (10). The rationale for our choice of the appropriate three Debye modes is based on these physical oscillator terms and the resulting good fit (Figure 2d,e). The three Debye modes can be rationalized by the three subunits: one associated with the phonon modes of the magnetic Eu chains and the other two corresponding to the phonon modes of the nonmagnetic P and S sublattices. These three subunits are expected to be energetically different from each other, as reflected in three different Debye temperatures (Table S8).

At $T < 4$ K, the heat capacity data of $Eu_2(P_2L_6)$ feature an upturn, signifying the onset of a Schottky anomaly.[44] The C_P/T data at $T \leq 13$ K were analyzed using eq 8.

$$C_{Sch} = k + \beta_3 T^3 + R\left(\frac{\Delta}{T}\right)^2 \frac{(g_0/g_1)e^{\Delta/T}}{[1 + (g_0/g_1)e^{\Delta/T}]^2} \tag{8}$$

where k is a mathematical constant and R is the gas constant. The first term accounts for the low-temperature Debye phonon, while the second term describes the two-level (g_0 and g_1) Schottky model. From the nonlinear fit, the gap between the energy levels, Δ, and the ratio of the ground-state population to the excited-state population, g_0/g_1, were extracted. As presented in Figure 2f and Table S9, Δ and g_0/g_1 increase as the applied magnetic field increases.[45,46]

Electronic transitions for the materials were studied through UV−vis−NIR spectroscopy.[47,48]

$$[\alpha(h\nu)]^{1/\gamma} = B(h\nu - E_g) \tag{9}$$

where $\alpha(h\nu)$ is the absorption coefficient, describing the relative rate of decrease in light intensity along its propagation path; h, the Planck constant; ν, photon frequency; γ, a factor describing the nature of the electronic transition, which equals 1/2 for direct band gaps and 2 for indirect band gaps; E_g, the band gap energy expressed in eV; and B, a constant.

Lanthanide materials tend to display sharp absorption peaks in UV−vis spectra owing to the buried nature of the 4f orbitals and more ionic bonding characters. The UV−vis spectra of $Eu_2(P_2L_6)$, however, show a rather broad feature of the absorption peak (Figure S9). The materials exhibit a direct band gap of 2.46 eV for $Eu_2(P_2S_6)$ and 1.99 eV for $Eu_2(P_2Se_6)$, consistent with their bright yellow and orange colors and with the previous report.[32] The absorption in the UV−vis−NIR spectra can be assigned to the spin-allowed $^8S_{7/2}$ ($4f^7$) → $^7F \otimes {}^1D$ ($4f^6 5d^1$) transition (Figure 3). While the electronic transition is typical for Eu^{2+} systems, it is worth noting that the colors of $Eu_2(P_2L_6)$ are more intense than those of other Eu^{2+} compounds (mostly colorless to light green colors). Our band

https://doi.org/10.1021/acsmaterialsau.4c00102
ACS Mater. Au XXXX, XXX, XXX−XXX

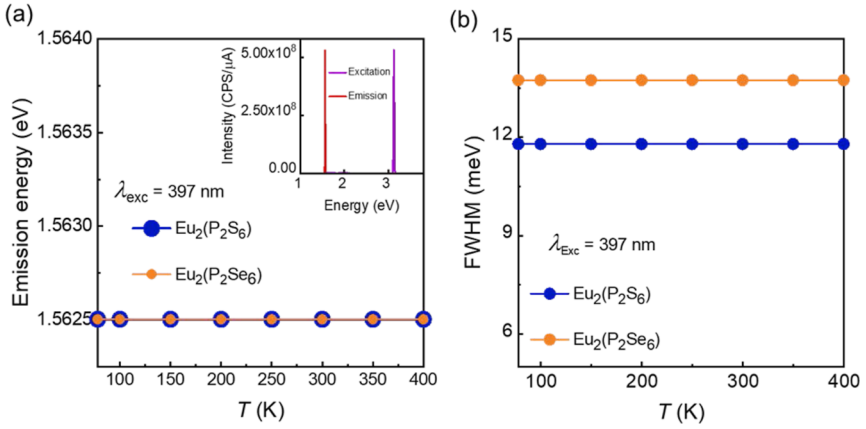

Figure 4. Temperature-dependent luminescence properties of $Eu_2(P_2S_6)$ and $Eu_2(P_2Se_6)$: (a) emission energy, inset: excitation and emission energy; (b) fwhm.

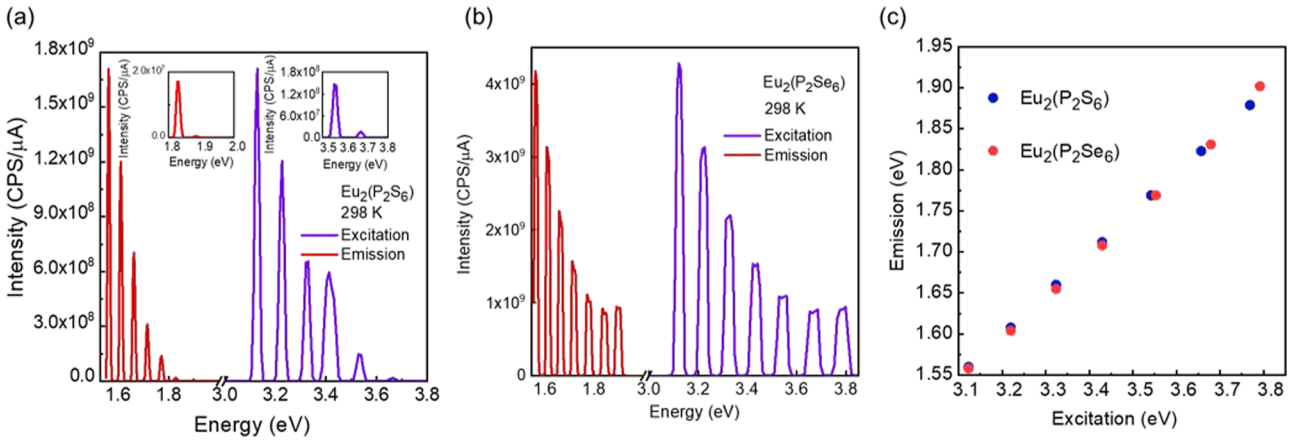

Figure 5. Emission and excitation spectra of (a) $Eu_2(P_2S_6)$ and (b) $Eu_2(P_2Se_6)$. The insets in (a) account for the tail end of the $Eu_2(P_2S_6)$ spectra, showing all seven transitions. (c) Resonance between the excitation and emission spectra of $Eu_2(P_2S_6)$ and $Eu_2(P_2Se_6)$.

structure and density of states calculations revealed that the conduction band minimum (CBM) is mainly dominated by L-p states. This low-lying band of the L ligand can facilitate a metal-to-ligand charge transfer Eu-4f → L-p (MLCT). The Se-4p states are more dispersed than the S-3p states, thus, lowering the energy of the CBM in $Eu_2(P_2Se_6)$. The combination of Eu-5d involvement in the electronic transition and a possible MLCT may explain broad features of the UV−vis spectra and the band gaps of $Eu_2(P_2L_6)$. The FTIR spectra of $Eu_2(P_2L_6)$ show 5 bands expected for bonding vibrations in $[P_2X_6]^{4-}$ groups in D_{3d} symmetry, $\Gamma_{vib} = 2A_{2u} + 3E_u$ (Figure S10 and Table S10). The shift of the P−P vibrational modes to higher frequencies in $Eu_2(P_2Se_6)$ can be attributed to the lower electron withdrawal from Se to the P−P bond than from S.

We investigated the luminescence properties of $Eu_2(P_2L_6)$ as a function of the temperature (Figure 4). At 298 K, the materials display narrow excitation and emission bands at 3.12 and 1.56 eV, respectively (Figure 4a, inset). At 78 K ≤ T ≤ 400 K, the emission energy and full width at half-maximum (fwhm) of $Eu_2(P_2L_6)$ remain the same as temperature changes. The insensitivity of the emission spectra to temperature indicates that there is no structural phase transition and no band adjustment within this temperature range. While the emission energy of $Eu_2(P_2S_6)$ falls exactly on top of that of $Eu_2(P_2Se_6)$, the fwhm is different. The Se material features a slightly broader fwhm, approximately 1.12 times that of the S compound. The more diffuse emission spectra of $Eu_2(P_2Se_6)$ can be attributed to the more dispersed Se-4p bands.

The absorption and emission processes in Eu^{2+} are dominated by 4f-5d electronic transitions.[49−53] The ground state involves the occupied $4f^7$ orbitals ($^8S_{7/2}$). Upon excitation of the Eu^{2+} ion in a crystal lattice, the $^7F \otimes {}^1D$ ($4f^6 5d^1$) excited state is generated, with multiplets of J = 0−6, at higher energy than the $4f^7(^6P_{7/2})$ state (Figure 3).[50,51,53,54] The energy difference between the 4f and 5d orbitals in Eu^{2+} is large, approximately 4.2−5.4 eV.[51,55,56] This implies that such optical transitions would occur in the UV region for a free Eu^{2+} ion. In a crystal lattice, however, relevant effects such as the nephelauxetic effect, crystal field splitting, and Stokes shifts decrease the energy gap toward red shift while strongly stabilizing the $^7F \otimes {}^1D$ excited-state manifold right above the $^8S_{7/2}$ ground state (Figure 3).[30,49,50] As such, depending on contributing factors, optically enabled transitions in Eu^{2+} systems can span from near-UV to near-IR wavelengths. The 4f orbitals are very localized and, consequently, have very minimal interactions with ligands.[49] When the 5d orbitals are populated, the nephelauxetic effect enhances the orbital overlap between the central lanthanide ion and ligands.[57] In a cubic crystal field, the electric field generated by the surrounding ligands lifts the degeneracy of the 5d orbitals. The energy difference between the two 5d orbital subsets is defined as crystal field splitting. Generally, a crystal field splitting

https://doi.org/10.1021/acsmaterialsau.4c00102
ACS Mater. Au XXXX, XXX, XXX−XXX

depends on the point symmetry of the lanthanide ion, bonding characters, and bond distances.[57] With regard to a C_{2v} symmetry, the degeneracy of the 5d orbital subsets is further broken, resulting in 5 states (Figure 3).[50]

To model the 4f-5d transitions, we assume that the interaction between the $4f^6$ electrons and the 5d electron in the $^7F\otimes{}^1D$ ($4f^65d^1$) excited state is negligible, and each orbital retains much of its intrinsic characteristics. The $4f^6$ electrons can be described in their $^{2S+1}L_J$ state, while 5d splits according to the ligand field symmetry up to 5 d-levels.[50] The $4f^6$ electrons may occupy any of the ^7F_J states and spread about 0.6 eV in energy.[53,58] Ideally, all 7 transitions associated with J = 0−6 states can be observed individually for absorption and emission processes in a "staircase" structure.[30,51,53,54] Usually, the "steps" of such "staircase" structures in excitation and emission spectra of Eu^{2+} are difficult to resolve.[53] This may be due to Eu^{2+}-doped concentration, local Eu^{2+} symmetry in a substrate, and Eu−L bonding characters.

Motivated by the stoichiometry of $Eu_2(P_2L_6)$, the C_{2v} crystal field, and the improved covalency of Eu−L bonds, we looked further into their narrow PL spectra. We observed a splitting of the excitation band with a 5−8 nm width. We then carefully repeated the excitation and emission processes at each new peak position. This measurement resulted in 7 peak positions (Table S11). Figure 5a,b shows "staircase" spectral features for the 7 excitation and 7 corresponding emission transitions in $Eu_2(P_2L_6)$. This feature is quite unique in that all 7 excitations and 7 emissions are observed individually for Eu(II).[51,53,54,58] This well-resolved PL is supported by the C_{2V} crystal field of Eu^{2+} in $Eu_2(P_2L_6)$ and more covalent Eu−L bonding characters, which effectively remove the degeneracy of the $^8S_{7/2}$ ground state and the $^7F\otimes{}^1D$ excited state.

The 7 excitation bands space evenly ∼0.11 eV from one another over an energy range of 0.64 eV for $Eu_2(P_2S_6)$ and 0.67 eV for $Eu_2(P_2Se_6)$. From the emission spectra, we also observed uniform spacing (∼0.05 eV) of the emission bands over an energy range of 0.31 eV for $Eu_2(P_2S_6)$ and 0.33 eV for $Eu_2(P_2Se_6)$. The difference in the spacing between the excitation and emission bands suggests the difference in the transition manifolds. While the excitation bands may reveal the J splitting of the A_1 state, the emission bands could address the broken degeneracy of the $^8S_{7/2}$ ground state into 7 states (Figure 3). Figure 5c depicts some degree of resonance between the excitation and emission processes in $Eu_2(P_2L_6)$. Overall, the excitation and emission energies display a linear correlation. The first 4 excitation and emission bands of $Eu_2(P_2L_6)$ have essentially the same energies. As the energy goes up further, there is some small difference between $Eu_2(P_2S_6)$ and $Eu_2(P_2Se_6)$ in their last 3 bands. This deviation increases as the energy increases. $Eu_2(P_2Se_6)$ exhibits slightly higher energy in the last 3 excitation and emission bands (Figure 5c). This could be explained by the impact of crystal field splitting and chemical bonds on the excitation and emission processes. Eu−Se bonds are longer than Eu−S bonds, leading to a smaller crystal field d-splitting in $Eu_2(P_2Se_6)$ than in $Eu_2(P_2S_6)$ (Figure 3). As a result, some excitation and emission bands of $Eu_2(P_2Se_6)$ are observed at a higher energy. We performed a preliminary time-resolved PL analysis for $Eu_2(P_2L_6)$ using an available excitation source operating at 375 nm (3.3 eV). At this excitation, an emission is observed at 773 nm (1.6 eV). The PL lifetime of $Eu_2(P_2S_6)$ and $Eu_2(P_2Se_6)$ is 31.93 and 32.37 ns, respectively (Figure S11). This lifetime is comparable to those of stoichiometric EuX_2 (X = Cl, Br, I) materials.[59,60]

To connect the electronic structure of $Eu_2(P_2L_6)$ to their magnetic and optical properties, we performed DFT calculation using a full-potential treatment of the electrons based on the augmented plane wave plus local orbital (APW + lo) method implemented in WIEN2k (Figures 6 and S14).[36]

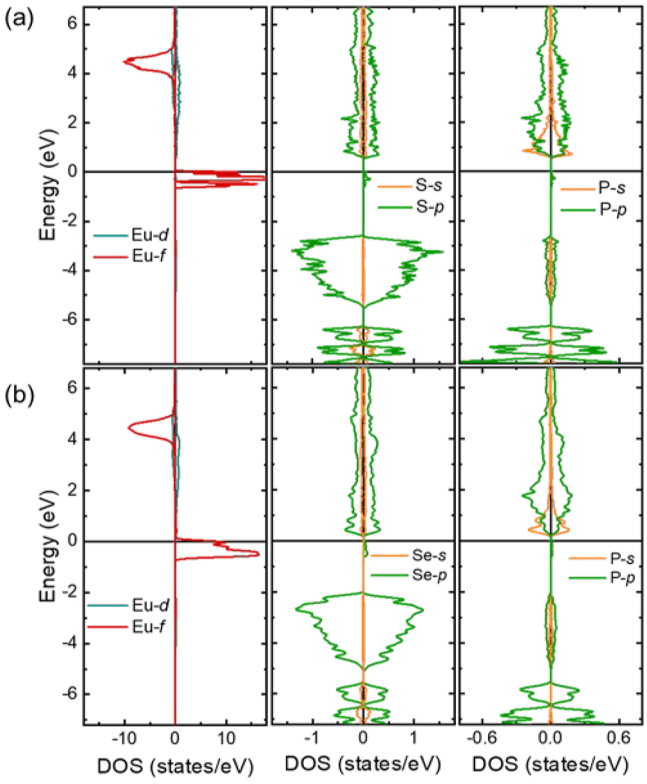

Figure 6. SP DFT calculations showing the partial density of states of (a) $Eu_2(P_2S_6)$ and (b) $Eu_2(P_2Se_6)$. The arrows indicate spin polarization (up and down).

With SP calculation and spin−orbit coupling, the Eu-4f states are polarized—direct evidence for magnetism. This confirms the paramagnetic behavior of $Eu_2(P_2L_6)$. The Eu-4f states are localized and make up mostly the valence band maximum (VBM). The P-, S-, and Se-states show some polarization and an appreciable contribution to the CBM. The Eu-5d states are more diffused than the Eu-4f states and couple with the Eu-4f states above the Fermi level, strongly supporting the $^7F\otimes{}^1D$ ($4f^65d^1$) excited-state manifold discussed in the PL results. When compared to the UV−vis absorption spectra, the calculated band gap is smaller: 0.47 eV for $Eu_2(P_2S_6)$ and 0.18 eV for $Eu_2(P_2Se_6)$. The difference lies in the tendency of the DFT calculations to underestimate the band gap. However, both $Eu_2(P_2S_6)$ and $Eu_2(P_2Se_6)$ present a direct band gap, with VBM and CBM located at wavevector X (Figure S14). The Se-4p bands are more dispersed and lower in energy in the CBM than the S-3p bands, underpinning the broader emission spectra and smaller band gap of $Eu_2(P_2Se_6)$.

CONCLUSIONS

Our results demonstrate an approach to creating and tuning optically responsive spin states in $Eu_2(P_2L_6)$ paramagnets. We show that the Eu^{2+} spin centers are magnetically isolated and exhibit ideal seven well-defined narrow transitions in the

https://doi.org/10.1021/acsmaterialsau.4c00102
ACS Mater. Au XXXX, XXX, XXX−XXX

excitation and emission spectra, which are nontrivial to resolve for Eu^{2+} systems. This realization is enabled by the stoichiometric $Eu_2(P_2L_6)$, symmetry, crystal field, and bonding characters in the materials. For future work, a thorough quantitative analysis of the PL spectral features will be conducted using computation. Detailed studies of the lifetime of each observed transition and magnetic relaxation behavior are underway. We envisage more insights into ligand field splitting, *g*-factor, and intramolecular interactions from electron paramagnetic resonance spectroscopy—vital information that is directly relevant to qubit design. Our work opens a pathway for addressing current fundamental challenges in material development for precisely accessing multiple spin states with light from simple, judicious refinements at the atomic and molecular levels.

■ ASSOCIATED CONTENT

Supporting Information

The Supporting Information is available free of charge at https://pubs.acs.org/doi/10.1021/acsmaterialsau.4c00102.

Additional data analysis, tables, and figures, including crystallographic data, TGA/DSC, FTIR, UV−vis, magnetization, heat capacity, excitation and emission and time-resolved PL, and SP band structures (PDF)

■ AUTHOR INFORMATION

Corresponding Author

Thao T. Tran − *Department of Chemistry, Clemson University, Clemson, South Carolina 29634, United States;* orcid.org/0000-0002-2395-3555; Email: thao@clemson.edu

Authors

Uchenna V. Chinaegbomkpa − *Department of Chemistry, Clemson University, Clemson, South Carolina 29634, United States*

Xudong Huai − *Department of Chemistry, Clemson University, Clemson, South Carolina 29634, United States*

Michal J. Winiarski − *Faculty of Applied Physics and Mathematics and Advanced Materials Center, Gdansk University of Technology ul. Narutowicza 11/12, Gdansk 80-233, Poland;* orcid.org/0000-0001-9083-8066

Hugo Sanabria − *Department of Physics and Astronomy, Clemson University, Clemson, South Carolina 29634, United States;* orcid.org/0000-0001-7068-6827

Complete contact information is available at: https://pubs.acs.org/10.1021/acsmaterialsau.4c00102

Author Contributions

Conceptualization: U.V.C; T.T.T. Data analysis: U.V.C.; X.H.; T.T.T. Resources: T.T.T. Preparation of original draft: U.V.C. Manuscript editing and review: U.V.C; X. H., M.J.W, H.S., T.T.T. Project supervision and administration: T.T.T. CRediT: **Uchenna V Chinaegbomkpa** conceptualization, data curation, formal analysis, methodology, visualization, writing - original draft.

Notes

The authors declare no competing financial interest.

■ ACKNOWLEDGMENTS

This work at Clemson University was supported by the National Science Foundation under Award NSF-OIA-2227933 and Award NSF-DMR-2338014. X.H. is supported by the Arnold and Mabel Beckman Foundation through a 2023 BYI award to T.T.T. We acknowledge funds from the Clemson Major Research Instrumentation (CU-MRI) initiative. We thank John Bacsa at Emory University for single-crystal X-ray data collection. The research at the Gdańsk University of Technology was supported by the National Science Centre (Poland) under the SONATA-15 grant (UMO-2019/35/D/ST5/03769).

■ REFERENCES

(1) Pedersen, K. S.; Ariciu, A.-M.; McAdams, S.; Weihe, H.; Bendix, J.; Tuna, F.; Piligkos, S. Toward molecular 4f single-ion magnet qubits. *J. Am. Chem. Soc.* **2016**, *138* (18), 5801−5804.

(2) Leuenberger, M. N.; Loss, D. Quantum computing in molecular magnets. *Nature* **2001**, *410* (6830), 789−793.

(3) Stepanenko, D.; Trif, M.; Loss, D. Quantum computing with molecular magnets. *Inorg. Chim. Acta* **2008**, *361* (14−15), 3740−3745.

(4) Gaita-Ariño, A.; Luis, F.; Hill, S.; Coronado, E. Molecular spins for quantum computation. *Nat. Chem.* **2019**, *11* (4), 301−309.

(5) Baldovi, J. J.; Cardona-Serra, S.; Clemente-Juan, J. M.; Coronado, E.; Gaita-Arino, A.; Palii, A. Rational design of single-ion magnets and spin qubits based on mononuclear lanthanoid complexes. *Inorg. Chem.* **2012**, *51* (22), 12565−12574.

(6) Coronado, E. Molecular magnetism: from chemical design to spin control in molecules, materials and devices. *Nat. Rev. Mater.* **2019**, *5* (2), 87−104.

(7) Oyeka, E. E.; Tran, T. T. Single-Ion Behavior in New 2-D and 3-D Gadolinium $4f^7$ Materials: $CsGd(SO_4)_2$ and $Cs[Gd(H_2O)_3(SO_4)_2]\cdot H_2O$. *ACS Org. Inorg. Au* **2022**, *2* (6), 502−510.

(8) Oyeka, E. E.; Winiarski, M. J.; Świątek, H.; Balliew, W.; McMillen, C. D.; Liang, M.; Sorolla, M.; Tran, T. T. Ln2 (SeO3) 2 (SO4)(H2O) 2 (Ln= Sm, Dy, Yb): A Mixed-Ligand Pathway to New Lanthanide (III) Multifunctional Materials Featuring Nonlinear Optical and Magnetic Anisotropy Properties. *Angew. Chem., Int. Ed.* **2022**, *61* (48), No. e202213499.

(9) Bode, B. E.; Fusco, E.; Nixon, R.; Buch, C. D.; Weihe, H.; Piligkos, S. Dipolar-coupled entangled molecular 4f qubits. *J. Am. Chem. Soc.* **2023**, *145* (5), 2877−2883.

(10) Moreno-Pineda, E.; Godfrin, C.; Balestro, F.; Wernsdorfer, W.; Ruben, M. Molecular spin qudits for quantum algorithms. *Chem. Soc. Rev.* **2018**, *47* (2), 501−513.

(11) Woodruff, D. N.; Winpenny, R. E. P.; Layfield, R. A. Lanthanide single-molecule magnets. *Chem. Rev.* **2013**, *113* (7), 5110−5148.

(12) Aguilà, D.; Roubeau, O.; Aromí, G. Designed polynuclear lanthanide complexes for quantum information processing. *Dalton Trans.* **2021**, *50* (35), 12045−12057.

(13) Dey, A.; Kalita, P.; Chandrasekhar, V. Lanthanide (III)-based single-ion magnets. *ACS Omega* **2018**, *3* (8), 9462−9475.

(14) Godfrin, C.; Ferhat, A.; Ballou, R.; Klyatskaya, S.; Ruben, M.; Wernsdorfer, W.; Balestro, F. Operating quantum states in single magnetic molecules: implementation of Grover's quantum algorithm. *Phys. Rev. Lett.* **2017**, *119* (18), 187702.

(15) Liu, Y.; Toma, F. M. Catalyst Qubits from the bottom up. *Chem* **2020**, *6* (4), 795−798.

(16) Bayliss, S. L.; Deb, P.; Laorenza, D. W.; Onizhuk, M.; Galli, G.; Freedman, D. E.; Awschalom, D. D. Enhancing spin coherence in optically addressable molecular qubits through host-matrix control. *Phys. Rev. X* **2022**, *12* (3), 031028.

(17) McAdams, S. G.; Ariciu, A.-M.; Kostopoulos, A. K.; Walsh, J. P. S.; Tuna, F. Molecular single-ion magnets based on lanthanides and

actinides: Design considerations and new advances in the context of quantum technologies. *Coord. Chem. Rev.* **2017**, *346*, 216−239.
(18) Tuna, F. Reaction: Molecular spins as qubits. *Chem* **2020**, *6* (4), 799−800.
(19) Atzori, M.; Sessoli, R. The second quantum revolution: role and challenges of molecular chemistry. *J. Am. Chem. Soc.* **2019**, *141* (29), 11339−11352.
(20) Gompa, T. P.; Greer, S. M.; Rice, N. T.; Jiang, N.; Telser, J.; Ozarowski, A.; Stein, B. W.; La Pierre, H. S. High-Frequency and-Field Electron Paramagnetic Resonance Spectroscopic Analysis of Metal−Ligand Covalency in a 4f7 Valence Series (Eu2+, Gd3+, and Tb4+). *Inorg. Chem.* **2021**, *60* (12), 9064−9073.
(21) Jenkins, M. D.; Duan, Y.; Diosdado, B.; García-Ripoll, J. J.; Gaita-Ariño, A.; Giménez-Saiz, C.; Alonso, P. J.; Coronado, E.; Luis, F. Coherent manipulation of three-qubit states in a molecular single-ion magnet. *Phys. Rev. B* **2017**, *95* (6), 064423.
(22) Handzlik, G.; Magott, M.; Arczyński, M.; Sheveleva, A. M.; Tuna, F.; Sarewicz, M.; Osyczka, A.; Rams, M.; Vieru, V.; Chibotaru, L. F.; et al. Magnetization dynamics and coherent spin manipulation of a propeller Gd (III) complex with the smallest helicene ligand. *J. Phys. Chem. Lett.* **2020**, *11* (4), 1508−1515.
(23) Luis, F.; Alonso, P. J.; Roubeau, O.; Velasco, V.; Zueco, D.; Aguilà, D.; Martínez, J. I.; Barrios, L. A.; Aromí, G. A dissymmetric [Gd2] coordination molecular dimer hosting six addressable spin qubits. *Commun. Chem.* **2020**, *3* (1), 176.
(24) Carlotto, S.; Babetto, L.; Bortolus, M.; Carlotto, A.; Rancan, M.; Bottaro, G.; Armelao, L.; Carbonera, D.; Casarin, M. Nature of the Ligand-Centered Triplet State in Gd^{3+}-β-Diketonate Complexes as Revealed by Time-Resolved EPR Spectroscopy and DFT Calculations. *Inorg. Chem.* **2021**, *60* (20), 15141−15150.
(25) Hu, Z.; Ullah, A.; Prima-Garcia, H.; Chin, S. H.; Wang, Y.; Aragó, J.; Shi, Z.; Gaita-Ariño, A.; Coronado, E. Binding Sites, Vibrations and Spin-Lattice Relaxation Times in Europium (II)-Based Metallofullerene Spin Qubits. *Chem.—Eur. J.* **2021**, *27* (52), 13242−13248.
(26) Errulat, D.; Harriman, K. L. M.; Gálico, D. A.; Salerno, E. V.; van Tol, J.; Mansikkamäki, A.; Rouzières, M.; Hill, S.; Clérac, R.; Murugesu, M. Slow magnetic relaxation in a europium (II) complex. *Nat. Commun.* **2024**, *15* (1), 3010.
(27) Joos, J. J.; Smet, P. F.; Seijo, L.; Barandiarán, Z. Insights into the complexity of the excited states of Eu-doped luminescent materials. *Inorg. Chem. Front.* **2020**, *7* (4), 871−888.
(28) Santanni, F.; Albino, A.; Atzori, M.; Ranieri, D.; Salvadori, E.; Chiesa, M.; Lunghi, A.; Bencini, A.; Sorace, L.; Totti, F.; et al. Probing vibrational symmetry effects and nuclear spin economy principles in molecular spin qubits. *Inorg. Chem.* **2020**, *60* (1), 140−151.
(29) De Laeter, J. R.; Böhlke, J. K.; De Bievre, P.; Hidaka, H.; Peiser, H. S.; Rosman, K. J. R.; Taylor, P. D. P. Atomic weights of the elements. Review 2000 (IUPAC Technical Report). *Pure Appl. Chem.* **2003**, *75* (6), 683−800.
(30) Adachi, S. Review−Photoluminescence Spectroscopy of Eu2+-Activated Phosphors: From Near-UV to Deep Red Luminescence. *ECS J. Solid State Sci. Technol.* **2023**, *12*, 016002.
(31) Freiser, M. J.; Methfessel, S.; Holtzberg, F. Multiplet structure in the absorption spectrum of Eu2+. *J. Appl. Phys.* **1968**, *39* (2), 900−902.
(32) Huang, X.; Yang, S. H.; Li, X. H.; Liu, W.; Guo, S. P. Eu2P2S6: The First Rare-Earth Chalcogenophosphate Exhibiting Large Second-Harmonic Generation Response and High Laser-Induced Damage Threshold. *Angew. Chem., Int. Ed.* **2022**, *61* (32), No. e202206791.
(33) Rigaku Oxford Diffraction *CrysAlisPro Software System*. Version 1.38.41; Rigaku, 2018.
(34) Sheldrick, G. M. SHELXT−Integrated space-group and crystal-structure determination. *Acta Crystallogr., Sect. A: Found. Adv.* **2015**, *71* (1), 3−8.
(35) Coelho, A. A. T. O. P. A. S. *TOPAS* and *TOPAS-Academic*: an optimization program integrating computer algebra and crystallographic objects written in C++. *J. Appl. Crystallogr.* **2018**, *51* (1), 210−218.
(36) Blaha, P.; Schwarz, K.; Tran, F.; Laskowski, R.; Madsen, G. K.; Marks, L. D. WIEN2k: An APW+ lo program for calculating the properties of solids. *J. Chem. Phys.* **2020**, *152* (7), 074101.
(37) Perdew, J. P.; Burke, K.; Ernzerhof, M. Generalized gradient approximation made simple. *Phys. Rev. Lett.* **1996**, *77* (18), 3865−3868.
(38) Broekner, W.; Becker, R. Eu2P2S6: Das erste Seltenerd-Thiohypodiphosphat. *Z. Naturforsch., A: Phys. Sci.* **1987**, *42* (5), 511−512.
(39) Jörgens, S.; Mewis, A.; Hoffmann, R. D.; Pöttgen, R.; Mosel, B. D. Neue Hexachalcogeno-Hypodiphosphate der Erdalkalimetalle und des Europiums. *Z. Anorg. Allg. Chem.* **2003**, *629* (3), 429−433.
(40) Gjikaj, M.; Ehrhardt, C. New Hexachalcogeno−Hypodiphosphates of the Alkali Metals: Synthesis, Crystal Structure and Vibrational Spectra of the Hexathiodiphosphate(IV) Hydrates $K_4[P_2S_6] \cdot 4\ H_2O$, $Rb_4[P_2S_6] \cdot 6\ H_2O$, and $Cs_4[P_2S_6] \cdot 6\ H_2O$. *Z. Anorg. Allg. Chem.* **2007**, *633* (7), 1048−1054.
(41) Shi, Z.-H.; Yang, M.; Yao, W.-D.; Liu, W.; Guo, S.-P. SnPQ3 (Q= S, Se, S/Se): A Series of Lone-pair Cationic Chalcogenophosphates Exhibiting Balanced NLO Activity Originating from SnQ8 Units. *Inorg. Chem.* **2021**, *60* (18), 14390−14398.
(42) Burdett, J. K. H.; HoffmannFay, R. R. C.; Robert, C. Eight-Coordination. *Inorg. Chem.* **1978**, *17* (9), 2553−2568.
(43) O'Handley, R. C. *Modern Magnetic Materials: Principles and Applications*; Wiley, 2000.
(44) Ahmet, T. *The Specific Heat of Matter at Low Temperatures*; Imperial College Press, 2003.
(45) Schüler, H.; Schmidt, T. Über abweichungen des atomkerns von der kugelsymmetrie. *Z. Phys.* **1935**, *94* (7−8), 457−468.
(46) Pichanick, F. M.; Sandars, P. G. H.; Woodgate, G. K. The nuclear magnetic dipole moments of the stable isotopes of europium and the hyperfine structure anomaly. *Proc. R. Soc. London, Ser. A* **1960**, *257* (1289), 277−282.
(47) Makuła, P.; Pacia, M.; Macyk, W. How to correctly determine the band gap energy of modified semiconductor photocatalysts based on UV−Vis spectra. *J. Phys. Chem. Lett.* **2018**, *9*, 6814−6817.
(48) Pankove, J. I. *Optical Processes in Semiconductors*; Courier Corporation, 1975.
(49) Teets, T. S. *Photoluminescence*; American Chemical Society, 2021.
(50) Sabbatini, N.; Ciano, M.; Dellonte, S.; Bonazzi, A.; Bolletta, F.; Balzani, V. Photophysical properties of europium (II) cryptates. *J. Phys. Chem.* **1984**, *88* (8), 1534−1537.
(51) Sugar, J.; Spector, N. Spectrum and energy levels of doubly ionized europium (Eu III). *J. Opt. Soc. Am.* **1974**, *64* (11), 1484−1497.
(52) Chen, Z.-X.; Liu, W.; Guo, S.-P. A review of structures and physical properties of rare earth chalcophosphates. *Coord. Chem. Rev.* **2023**, *474*, 214870.
(53) Dorenbos, P. A review on how lanthanide impurity levels change with chemistry and structure of inorganic compounds. *ECS J. Solid State Sci. Technol.* **2013**, *2* (2), R3001−R3011.
(54) Dorenbos, P. f→ d transition energies of divalent lanthanides in inorganic compounds. *J. Phys.: Condens. Matter* **2003**, *15* (3), 575−594.
(55) Dorenbos, P. Relation between Eu^2 and Ce^3 f d-transition energies in inorganic compounds. *J. Phys.: Condens. Matter* **2003**, *15* (27), 4797−4807.
(56) Qiao, J.; Zhou, G.; Zhou, Y.; Zhang, Q.; Xia, Z. Divalent europium-doped near-infrared-emitting phosphor for light-emitting diodes. *Nat. Commun.* **2019**, *10* (1), 5267.
(57) Wang, S.; Song, Z.; Kong, Y.; Xia, Z.; Liu, Q. 5d-level centroid shift and coordination number of Ce3+ in nitride compounds. *J. Lumin.* **2018**, *200*, 35−42.
(58) Dorenbos, P. Energy of the first 4f7→ 4f65d transition of Eu2+ in inorganic compounds. *J. Lumin.* **2003**, *104* (4), 239−260.
(59) Su, H.; Jia, Z.; Shi, C.; Xin, J.; Reid, S. A. 6P7/2-Excited-State Decay Mechanism and Energy-Transfer Processes in KMgF3: Eu2+

https://doi.org/10.1021/acsmaterialsau.4c00102
ACS Mater. Au XXXX, XXX, XXX−XXX

and KMgF3: Eu− X (X= Gd, Ce, Cr). *Chem. Mater.* **2001**, *13* (11), 3969−3974.
(60) Galimov, D. I.; Bulgakov, R. G. The first example of fluorescence of the solid individual compounds of Eu2+ ion: EuCl2, EuI2, EuBr2. *Luminescence* **2019**, *34* (1), 127−129.

https://doi.org/10.1021/acsmaterialsau.4c00102
ACS Mater. Au XXXX, XXX, XXX−XXX